DOI: 10.1002/ ((please add manuscript number))
Article type: Full Paper

In-situ formation of bismuth-based perovskite heterostructures for high-performance co-catalyst-free photocatalytic hydrogen evolution

*Yunqi Tang, Chun Hong Mak, Rugeng Liu, Xu Han, Zuankai Wang, Haisheng Song, Chunyan Tan, Frédéric Barrière and Hsien-Yi Hsu**

Y. Tang, R. Liu, C. H. Mak, X Han, Dr. H-Y Hsu
School of Energy and Environment & Department of Materials Science and Engineering
City University of Hong Kong, Kowloon Tong, Hong Kong, China
E-mail: sam.hyhsu@cityu.edu.hk

Y. Tang, R. Liu, C. H. Mak, X Han, Dr. H-Y Hsu
Shenzhen Research Institute of City University of Hong Kong,
Shenzhen 518057, China

Zuankai Wang
Department of Mechanical Engineering, City University of Hong Kong, Hong Kong, China.

Haisheng Song
Wuhan National Laboratory for Optoelectronics (WNLO) and School of Optical and Electronic Information, Huazhong University of Science and Technology
1037 Luoyu Road, 430074, Wuhan, Hubei, P. R. China

Chunyan Tan
The Graduate School at Shenzhen, Tsinghua University, Shenzhen, Guangdong 518055, China.

Frédéric Barrière
Univ Rennes, CNRS, ISCR (Institut des Sciences Chimiques de Rennes) – UMR 6226, F-35000 Rennes, France.

Keywords: in-situ formation, perovskite heterojunction, co-catalyst-free, photocatalytic hydrogen evolution

ACCEPTED MANUSCRIPT

Solar-to-fuel conversion with organic-inorganic hybrid halide perovskites has attracted growing attention, as a result of conspicuous optoelectronic properties as well as the low-temperature solution process. However, the most comprehensively developed hybrid perovskite materials comprise the toxic metal lead, raising concerns about their environmental health threats. Herein, we successfully develop an environmentally friendly bismuth (Bi)-based hybrid perovskite with the in-situ growth of a heterojunction at the interface of methylammonium bismuth iodide ($MA_3Bi_2I_9$) and tri(dimetylammonium) hexa-iodobismuthate (DMA_3BiI_6) by a facile solvent engineering technique. The air-stable $MA_3Bi_2I_9/DMA_3BiI_6$ perovskite heterostructure with enhanced photoinduced charge separation exhibits outstanding visible-light-induced photocatalytic activity for H_2 evolution in aqueous HI solution. Powdered $MA_3Bi_2I_9/DMA_3BiI_6$ heterostructured composite (BBP-5) shows a H_2 evolution rate of 198.2 μmol $h^{-1}g^{-1}$ without the addition of Pt cocatalysts under 100 mW cm^{-2} visible-light ($\lambda \geq 420$ nm) illumination.

1. Introduction

Solar-driven hydrogen production induced by photocatalysts has been dramatically developed since the overall photocatalytic water splitting using a titanium dioxide electrode firstly reported by Honda and Fujishima in 1972.[1] Countless efforts for the direct conversion of solar energy to hydrogen fuels have been directed through photoelectrocatalytic and photocatalytic processes.[2] Due to nontoxicity, high photostability, cost effectiveness, and efficient photocatalytic activity, titanium dioxide (TiO_2) and graphitic carbon nitride (g-C_3N_4) photoactive semiconductors have been intensively investigated.[3] Nevertheless, unfavorable photocatalytic properties, e.g., high electron-hole recombination rate, narrow photoresponse range and low quantum efficiency could possibly confine their practical applications.[4] In recent years, organic-inorganic hybrid perovskites have been extensively utilized in solar energy conversion by virtue of remarkable photoelectric effect and extraordinary photovoltaic

ACCEPTED MANUSCRIPT

performance.[2c, 5] Strikingly, significant breakthroughs have been achieved in lead-based hybrid perovskite solar cells with a power conversion efficiency of 25.2% in 2019,[6] arising from their intrinsic properties, such as high absorption coefficient,[7] low exciton binding energy,[8] long carrier lifetime,[9] and so forth, which are definitely beneficial for photocatalytic hydrogen production.

Though the progress of lead-based hybrid perovskites for solar-to-electricity has been attained, hybrid perovskite semiconductors are highly moisture sensitive, giving rise to the degradation in water. Thus, this introduced a significant challenge for H_2 evolution with hybrid perovskite photocatalysts in an aqueous solution. To overcome this stability issue, Park et al. adopted methylammonium lead iodide ($MAPbI_3$) photocatalysts using Pt as a co-catalyst in dynamic equilibrium of a saturated aqueous solution for hydrogen iodide (HI) splitting, reaching a solar-to-hydrogen conversion efficiency of 57$\mu mol\ h^{-1}g^{-1}$) under visible light irradiation.[10] In 2018, Wu and co-workers prepared the $MAPbI_3$ composite combined with reduced graphene oxide for visible-light-driven H_2 evolution in aqueous HI solution.[11] Later, the incorporation of $MAPbI_3$ into Pt-loaded TiO_2 acted as a hybrid system to produce H_2 in aqueous HI solution.[12] In addition, a lead-free hybrid perovskite-like material, DMA_3BiI_6, without the loading of Pt co-catalysts showed poor photocatalytic rate (~15.16 $\mu mol\ h^{-1}g^{-1}$) for H_2 production in aqueous HI solution.[13] Followed by decorating DMA_3BiI_6 with platinum metals, the PtI_x/DMA_3BiI_6 hybrid structure was formed to improve the quantum efficiency of photocatalytic hydrogen production. Similarly, the deposition of Pt cocatalysts on the surface of $MA_3Bi_2I_9$ retained adequate phase stability, together with the enhancement of solar-to-chemical conversion efficiency while compared to the pure $MA_3Bi_2I_9$ perovskites.[14] Nevertheless, the photocatalytic performance of pristine hybrid perovskites without the use of any noble metal co-catalyst is absolutely unsatisfactory. On the basis of previous studies on typical photocatalysts, the construction of heterojunction structures to enhance charge separation and photocatalytic activity has been reported for hydrogen generation by the reason

ACCEPTED MANUSCRIPT

of energy band alignment across the interface of phase junction.[15] Herein, we present an in-situ generation of heterojunctions comprising $MA_3Bi_2I_9$ and DMA_3BiI_6 hybrid perovskites determined by scanning electron microscopy (SEM) and X-ray photoelectron spectroscopy (XPS) through a dimethylformamide (DMF)-assisted solvent-engineering technique. In the solvothermal synthesis, the isopropanol (IPA) was employed as a solvent with the addition of DMF as a co-solvent to tune the solvent polarity for achieving the solvation of methylammonium iodide (MAI) as well as the dispersion of bismuth nitrate ($Bi(NO_3)_3$). DMF is hydrolyzed in the reaction process while 5 volume percent of the DMF co-solvent is added in IPA solution. By utilizing time-resolved photoluminescence technique (TRPL) and electrochemical impedance spectroscopy (EIS), we confirm that air-stable $MA_3Bi_2I_9/DMA_3BiI_6$ perovskite heterojunctions can reinforce the efficiency of photogenerated carrier separation and transport, eventually leading to enhanced solar HI splitting efficiency in the absence of any noble metal co-catalyst.

2. Result and Discussion

2.1. Synthesis and morphology.

Figure 1a, b illustrates the simplified experimental procedure as well as the optical photographs of all the samples prepared by adding different amounts of the DMF co-solvent. In the photographs of these products, the colors from BBP-0 to BBP-10 gradually turn from dark red to light orange. The macro appearance of BBP-0 is tinsel-sheet-like, but the BBP-10 transfers to totally needle- or rod-like crystals while 10 volume percent (10 vol%) of the DMF co-solvent in IPA solution is added. As confirmed by the SEM images (**Figure 1c-f**), BBP-0 obviously possesses hexagonal two-dimensional sheet-like structure without the addition of any DMF co-solvent. By adding 1 vol% of DMF, the BBP-1 still maintains two-dimensional layered structure, but not perfectly hexagonal anymore (**Figure 1d**). While the amount of DMF is increased to 5 vol% into the solvothermal system, the overall contour is similar to BBP-1, but

ACCEPTED MANUSCRIPT

tight rod-like crystals are clearly visible on the surface in **Figure 1e**, possibly constructing the perovskite junctions across the interface of rod-like and sheet-like structures. When the amount of DMF in the reaction solution reaches 10 vol%, the obtained products are almost entirely single rod-like structure (**Figure 1f**). This observation is consistent with the results obtained from optical photographs of all the samples. In other words, varying amounts of added DMF as the co-solvent lead to different chemical reaction pathways during the solvothermal process, finally producing Bi-based hybrid perovskites with different morphologies. Specifically, the in-situ heterojunctions can be introduced into the final products by adding specific amount of the DMF co-solvent.

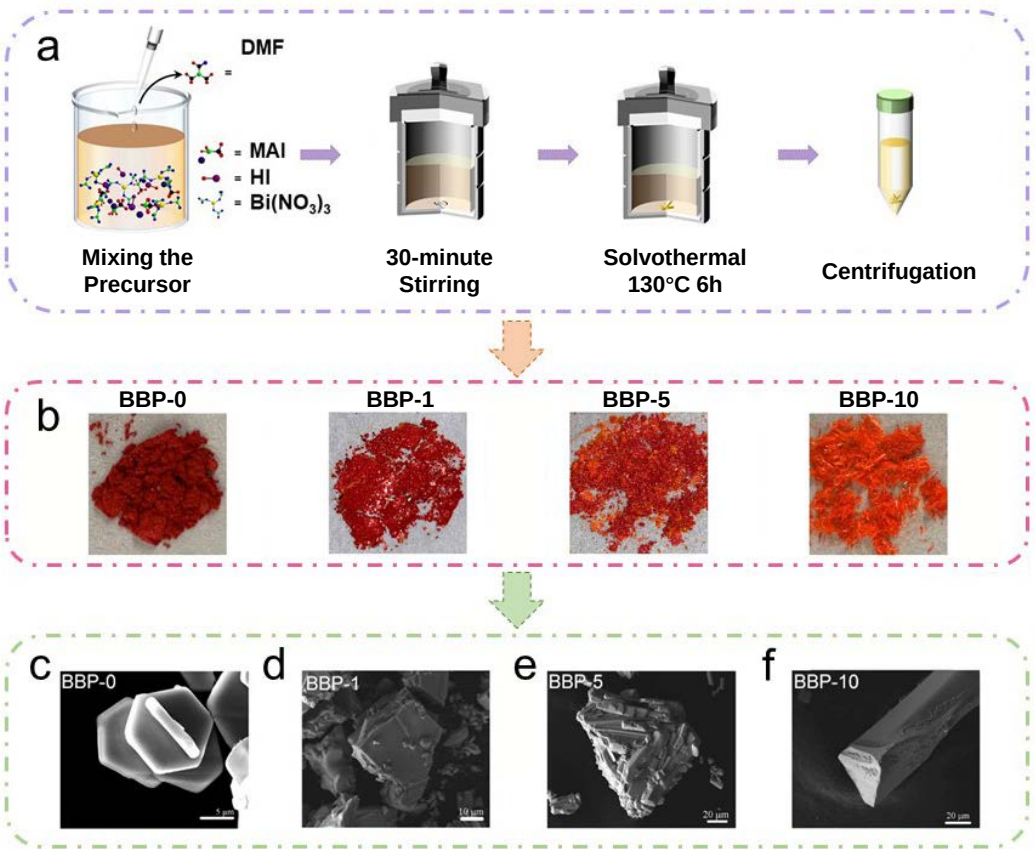


Figure 1. (a), The preparation process of BBP-x samples with the (b), photographs of precipitated samples. SEM images of (c), BBP-0, (d), BBP-1, (e), BBP-5 and (f), BBP-10.

ACCEPTED MANUSCRIPT

2.2. Materials characterization and crystal structure

X-ray diffraction (XRD) was conducted to characterize this series of bismuth-based perovskites (BBPs) powders, as well as BBP-0 and BBP-10 single crystals (**Figure 2a**). The single crystal diffraction data of BBP-0 reveals the structure of methylammonium bismuth iodide ($MA_3Bi_2I_9$ or $(CH_3NH_2)_3Bi_2I_9$), to be hexagonal (space group = P63/mmc), with unit cell parameters of a = 8.5843(12) Å, b = 8.5843(12) Å, c = 21.690(4) Å, α = 90.0, β = 90.0, and γ = 120.0 (**Table S1**). According to crystal data and structure refinement of $MA_3Bi_2I_9$ in **Table S1**, each unit cell contains two molecules with the chemical formula of $MA_3Bi_2I_9$. The unit cell of $MA_3Bi_2I_9$ comprises two isolated face-sharing $Bi_2I_9^{3-}$ octahedra encompassed by methylammonium cations (**Figure 2b**). The BBP-10 single crystals show the structure of tri (dimetylammonium) hexa-iodobismuthate (DMA_3BiI_6 or $[(CH_3)_2NH_2]_3[BiI_6]$) to be rhomboedric (space group = $R\bar{3}$), with unit cell parameters of a = 30.7543(15) Å, b = 30.7543(15) Å, c = 8.7945(5) Å, α= 90.0, β = 90.0, and γ = 120.0 (**Table S2**). Similarly, each unit cell containing twelve molecules with the chemical formula of DMA_3BiI_6 could be clarified by crystal data and structure refinement in **Table S2**. The crystal structure of DMA_3BiI_6 contains isolated BiI_6^{3-} octahedra surrounded by dimethylamine cations, as shown in **Figure 2c**. In terms of the powder XRD patterns, the diffraction peaks of the BBP-0 and BBP-10 powders are nearly identical to their calculated patterns from single crystal diffraction data, which are in good agrreement with previously reported data.[33-34] The main peaks for BBP-0 ($MA_3Bi_2I_9$) at 11.9°, 12.6°, 14.4°, 16.5°, 23.7°, 24.3°, 25.9°, 28.0° are assigned to the (100), (101), (102), (103), (006), (202), (203) and (204) lattice planes, respectively.[33, 35] For BBP-10 (DMA_3BiI_6), the evident peaks at 11.5°, 12.°, 16.7°, 17.7°, 24.9°, 25.2°, 25.5° are assigned to the (4 20), (201), (401), (531), (532), (810), and (701) planes. The XRD pattern of BBP-1 is similar to that of BBP-0, suggesting that the major component in BBP-1 is still $MA_3Bi_2I_9$ perovskites. While DMF/IPA volume percent of 5% is reached by adding DMF co-solvent, the characteristic perovskite doublet peak of BBP-5 at 2θ = ~ 12 ° is analogous to that of BBP-10.

ACCEPTED MANUSCRIPT

Besides, the triplet peaks at 2θ = ~ 25.3° become more obvious in BBP-5, indicating the products gradually transform from $MA_3Bi_2I_9$ to DMA_3BiI_6 as the amount of DMF in the incipient reaction solution increases. In other words, the existence of heterostructured $MA_3Bi_2I_9$/DMA_3BiI perovskites in BBP-5 is characterized. To further explore the chemical structure of this series of bismuth-based perovskites, Flourier transformed infrared spectroscopy (FTIR) was performed. As shown in **Figure 2d**, the signals at 3109cm^{-1} and 2950 cm^{-1} are attributed to the stretching vibrations of the N-H and C-H. The characteristic signal at 1082 cm^{-1} corresponds to the carbonyl group vibrations of formic acid produced by the hydrolysis of DMF.[36] The XRD profiles of bismuth-based perovskite, BBP-5, were investigated over a period of two months (**Figure 2e**). We observe that peak positions and/or intensities are almost the same, demonstrating the admirable atmospheric stability of this perovskite material under ambient conditions.

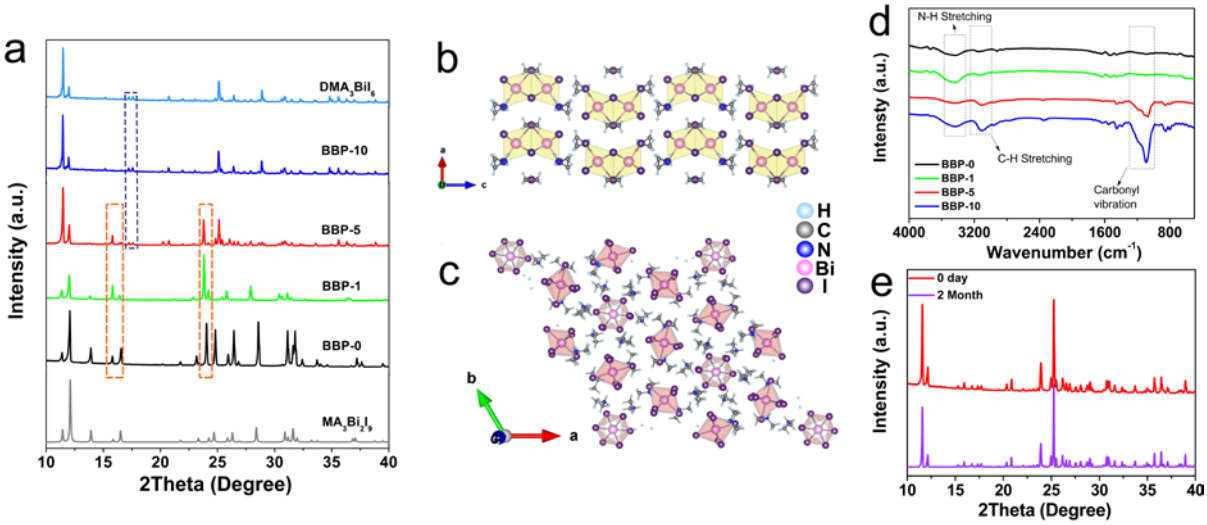


Figure 2. (a) X-ray diffraction (XRD) patterns of a series of bismuth-based perovskites as well as single-crystal $MA_3Bi_2I_9$ (BBP-0) (bottom) (grey) and DMA_3BiI_6 (BBP-10) (top) (light blue). Crystal structure of (b), $MA_3Bi_2I_9$ (BBP-0) and (c), DMA_3BiI_6 (BBP-10). The colors represent the following: pink, Bi ion; purple, I ion; dark grey, C ion; blue, N ion, light blue, H ion. (d), FT-IR spectra of all Bi-based perovskites. (e), Powder X-ray diffraction patterns of BBP-5 over a period of two months under ambient atmosphere.

ACCEPTED MANUSCRIPT

2.3. Proposed chemical reaction

Based on the above analysis of experimental results, the chemical reactions for the formation of BBP-0 ($MA_3Bi_2I_9$) and BBP-10 (DMA_3BiI_6) are proposed. Without the addition of DMF co-solvent in the system, the precursors, i.e., CH_3NH_2I (MAI), $Bi(NO_3)_3$ and HI, would directly react together during the solvothermal process, as presented in **Equation 1**

$$3CH_3NH_2I + 2Bi^{3+} + 6I^- \rightarrow (CH_3NH_2)_3Bi_2I_9 \text{ (or } MA_3Bi_2I_9) \quad (1)$$

As a matter of fact, the IPA and HI used in the experiment still contain a certain amount of water, DMF is reactive in water-containing systems and undergoes an hydrolytic reaction. Accordingly, in the solvothermal process, DMF ($(CH_3)_2NCOH$) would react with water to generate dimethylamine ($(CH_3)_2NH$) and formic acid (HCOOH) (**Equation 2**). In the meanwhile, due to the existence of H^+ in the system containing hydrogen iodide (HI), the $(CH_3)_2NH$ could be protonated to form $[(CH_3)_2NH_2]^+$ (DMA^+) ions (**Equation 3**).[16]

$$(CH_3)_2NCOH + H_2O \rightarrow (CH_3)_2NH + HCOOH \quad (2)$$

$$(CH_3)_2NH + H^+ \rightarrow [(CH_3)_2NH_2]^+ \quad (3)$$

$$3[(CH_3)_2NH_2]^+ + Bi^{3+} + 6I^- \rightarrow [(CH_3)_2NH_2]_3[BiI_6] \text{ (or } DMA_3BiI_6) \quad (4)$$

During the preparation of BBP-5 with $MA_3Bi_2I_9/DMA_3BiI_6$ heterojunctions, at the earliest stage, we observed that CH_3NH_2I effectively reacted with Bi^{3+} ions in the solution at room temperature, thus producing a portion of $MA_3Bi_2I_9$ in the pre-reaction solution prior to the solvothermal system, as illustrated in the step (I) of **Figure 3a**. By adding 5 vol% DMF in the solvothermal process, the unreacted bismuths were absorbed on the surface of preformed $MA_3Bi_2I_9$ perovskites, as confirmed by **Figure 3c**. The protonated amine $[(CH_3)_2NH_2]^+$ (DMA^+) ions generated through DMF hydrolysis then reacted with the unreacted bismuth ions on $MA_3Bi_2I_9$ perovskites (step II of **Figure 3a**), resulting in the in-situ formation of $MA_3Bi_2I_9/DMA_3BiI_6$ perovskite heterojunctions in BBP-5 (step III of **Figure 3a**), as determined by SEM (**Figure 1c-f**), XRD (**Figure 2a**) and XPS (**Figure 3b-d**). While the amount

ACCEPTED MANUSCRIPT

of DMF reaches to 10 vol% of the whole system, the $[(CH_3)_2NH_2]^+$ (DMA^+) cations were dominant in the solvothermal reaction to finally produce $DMA_3[BiI_6]$ perovskites (**Equation 4**).[17]

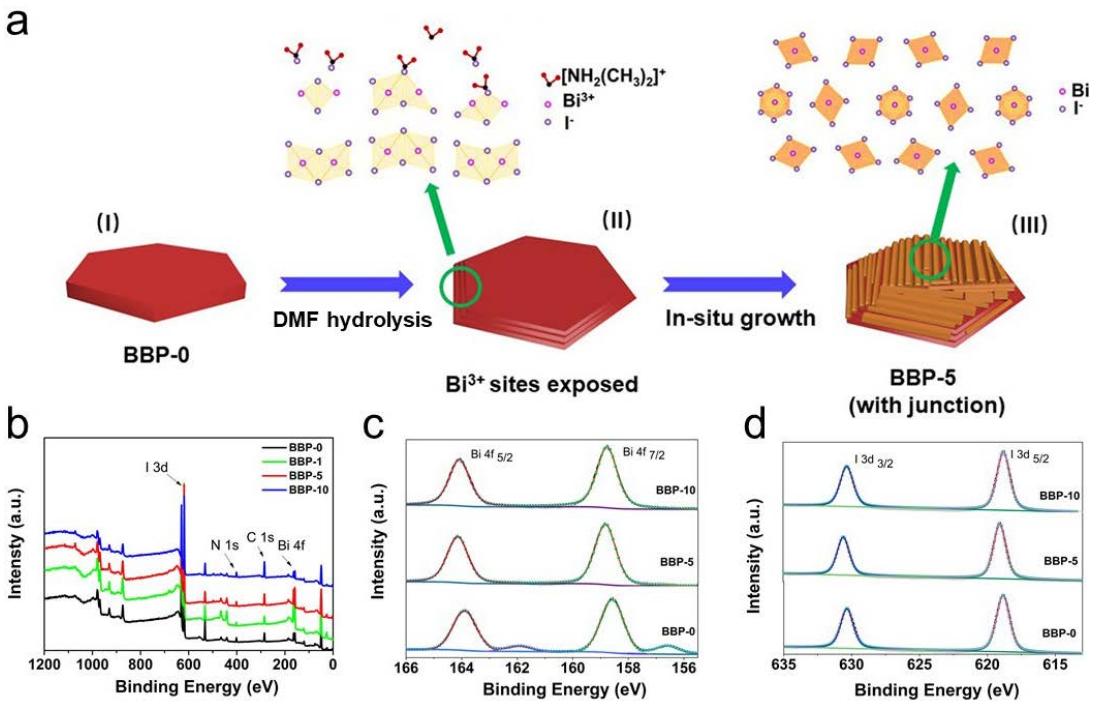


Figure 3. (a) Illustrated scheme of the formation of $MA_3Bi_2I_9/DMA_3BiI_6$ heterojunctions. (b), XPS survey spectra of all Bi-based perovskites. High-resolution XPS spectra of the (c)**,** Bi 4f and (d)**,** I 3d regions for BBP-0, BBP-5 and BBP-10.

To further verify the elemental composition, X-ray photoelectron spectroscopy (XPS) was performed for each compound (**Figure 3b-d and Figure 1**). On the basis of the full survey spectrum, the elements contain Bi, I, N, and C in BBP-0, BBP-1, BBP-5 and BBP-10 (**Figure 3b**). High-resolution XPS spectra of BBP-0, BBP-5 and BBP-10 for C 1s, and N 1s are presented in **Figure 1**. The peak detected at 284.8 eV is attributed to the C–C bond originating from the adventitious carbon.[18] Besides, the shoulder peak located at 285.9 eV is corresponding to the C–N bond of MA^+ and DMA^+.[19] **Figure 3c,d** show the high-resolution XPS spectra of Bi 4f and I 3d of BBP-0, BBP-5 and BBP-10. The characteristic peaks for Bi 4f are attributed to Bi $4f_{5/2}$ at 164 eV as well as Bi $4f_{7/2}$ at 158.7eV. Particularly, due to the

ACCEPTED MANUSCRIPT

reduction of iodobismuthates, the metallic bismuth at 161.8 eV and 156.5 eV in BBP-0 can be observed, indicating that some unreacted bismuths are absorbed on the surface of $MA_3Bi_2I_9$[20] and thus provide reactive sites for the subsequent chemical reaction with DMA^+ produced by the hydrolysis of DMF for the final generation of the $MA_3Bi_2I_9/DMA_3BiI_6$ heterojunctions in BBP-5, which is in agreement with proposed chemical reactions (**Equation 1-4**). In **Figure 3**d, the primary signals of I 3d at 630.3 eV and 618.8 eV are corresponding to I 3d3/2 and I 3d5/2, which is in line with the previous report.[21]

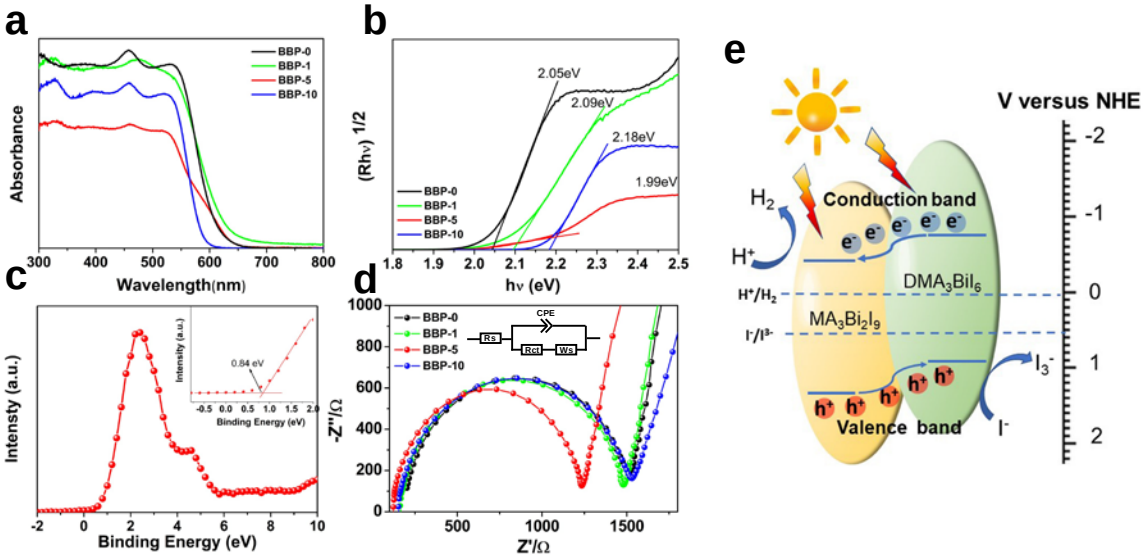


Figure 4. (a) UV–vis diffuse reflectance spectra and (b), indirect-bandgap Tauc plot of all as-prepared samples. (c) Valence level spectrum of the BBP-5 powders measured by XPS. Inset: linear analysis applied to the XPS valence band. (d) Nyquist plots of all prepared samples measured at 0 V versus Ag/AgCl electrode under light irradiation in dichloromethane solution containing 0.1 M tetrabutylammonium hexafluorophosphate ($TBAPF_6$) as electrolyte solution. Inset: equivalent circuit of the electrochemical cell. (e) Energy level diagram of the BBP-5 with a heterojunction of $MA_3Bi_2I_9$ and DMA_3BiI_6 for the photocatalytic HI splitting.

2.4. Photophysical and electrochemical properties

UV–vis diffuse reflectance spectroscopy and X-ray photoelectron (XPS) spectroscopy valence band spectroscopy were carried out to construct the band structure of all prepared

ACCEPTED MANUSCRIPT

powder samples. As shown in **Figure 4a**, all samples exhibit a wide range of visible light absorption from 300 nm to 650 nm. By Tauc plot using the Kubelka–Munk function in **Figure 4**b[21a, 22] we then determine the optical bandgap energy of all powder samples, in which the BBP-0, BBP-5 and BBP-10 perovskites reveal the absorption band edges at approximately 605, 623 and 569 nm, corresponding to the estimated band gaps (Eg) of 2.05, 1.99 and 2.18 eV respectively, which are suitable for the visible light-induced photocatalytic reaction. To demonstrate the valence band position, XPS valence band analyses of as-prepared samples were performed in **Figure 4c** and **Figure S2**. The energy positions of valence band maximum (VBM) of BBP-0, BBP-5 and BBP-10 are located at about 1.02, 0.84 and 0.80 eV *versus* the vacuum level. On a basis of the reported method,[22-23] the positions of VBM and conduction band minimum (CBM) are determined to be − 5.32/− 3.27, − 5.14/− 3.15, − 5.10/−2.92 eV for BBP-0 ($MA_3Bi_2I_9$), BBP-5 ($MA_3Bi_2I_9$/DMA_3BiI_6) and BBP-10 (DMA_3BiI_6) respectively, as schematically illustrated in **Figure 4e**. With respect to the normal hydrogen electrode (NHE), the VBM of $MA_3Bi_2I_9$ is more positive than that of DMA_3BiI_6 while the CBM of DMA_3BiI_6 is more negative than that of $MA_3Bi_2I_9$. A driving force for the separation of photogenerated charge carriers can therefore be provided by heterojunction band alignment of $MA_3Bi_2I_9$ and DMA_3BiI_6 with the consideration of thermodynamic aspects, i.e., the photoexcitation results in electron transportation from the conduction band of DMA_3BiI_6 to that of $MA_3Bi_2I_9$; in the meanwhile, the holes on the valance bands migrate in the opposite direction (**Figure 4e**). Accordingly, the BBP-5 perovskites with $MA_3Bi_2I_9$/DMA_3BiI_6 heterojunctions are highly potential for hydrogen reduction and iodine oxidation as a result of enhanced spatial charge separation.

To demonstrate the efficient charge separation at the interface of $MA_3Bi_2I_9$/DMA_3BiI_6, electrochemical impedance spectroscopy (EIS) was performed at open-circuit potential under visible light irradiation, as depicted in **Figure 4d**. The EIS Nyquist plots of all prepared samples were then simulated to the equivalent electrical circuit, as displayed in the inset of **Figure 4d**.

ACCEPTED MANUSCRIPT

In this model, the charge transfer resistance (R_{ct}) at the electrode-electrolyte interface, series resistance (R_s), constant phase element (CPE), as well as Warburg impedance (Z_W) are included in the circuit elements.[24] The charge transfer process at the electrode-electrolyte interface results in the high-frequency semicircle, while the diffusion process of the reactive species in the electrolyte leads to the low frequency arc.[25] **Table S3** shows the results of the Nyquist plots fitted based on the equivalent circuit diagram, exhibiting that the arc radii of BBP-5 composites with the $MA_3Bi_2I_9/DMA_3BiI_6$ heterojunction are much smaller than that of other Bi-based perovskites, i.e., heterostructured $MA_3Bi_2I_9/DMA_3BiI_6$ composite possesses a lower charge separation resistance than others, thereby inferring an evident improvement of the charge separation and transfer process between the interface of $MA_3Bi_2I_9/DMA_3BiI_6$.[26]

2.5 Photocatalytic performance of heterostructured Bi-based perovskites

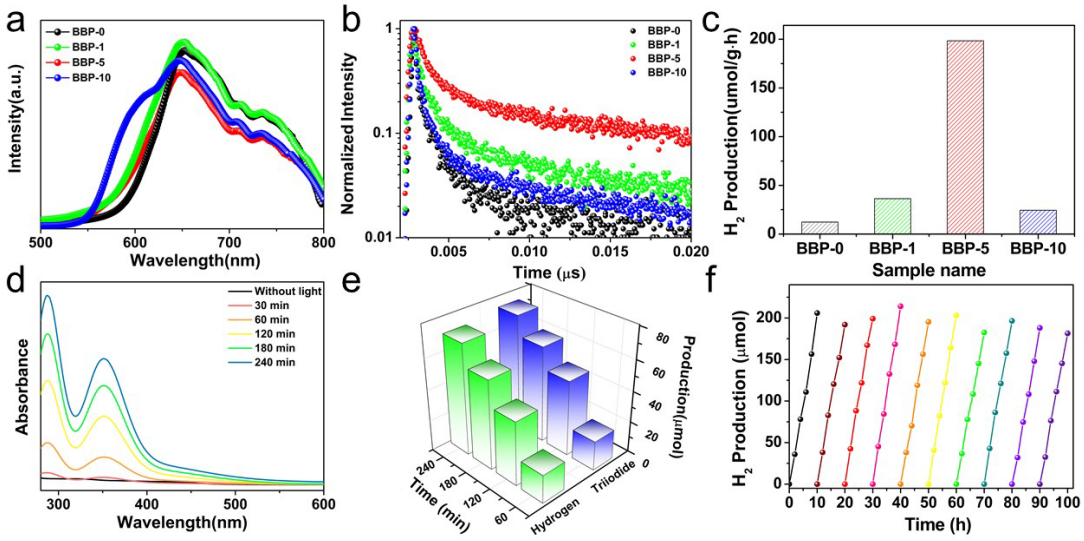


Figure 5. (a) Steady-state photoluminescence (PL) spectra with the excitation wavelength at 375nm. (b) Time-resolved photoluminescence (TRPL) spectra monitored at 650 nm. (c) Photocatalytic H2 production of all precipitated powder samples in HI saturated solution. (d) Time-dependent UV–Vis spectra of I^{3-} for photocatalytic HI splitting reaction of BBP-5. (e) Quantitative comparison between the evolved H_2 (green) and I^{3-} (purple) with the BBP-5

ACCEPTED MANUSCRIPT

photocatalyst. (f) Stable photocatalytic H_2 evolution produced by the BBP-5 powder in the saturated solution for 100 h. H_3PO_2 was added to the HI solution.

Steady-state photoluminescence (PL) spectra of all solid-state samples were obtained using an excitation wavelength of 450 nm, as presented in **Figure 5a.** Among the Bi-based perovskites, BBP-5 perovskite exhibits the lowest PL peak intensity, implying the suppression of photogenerated charge recombination, arising from the enhanced charge diffusion rate at the interface of $MA_3Bi_2I_9/DMA_3BiI_6$ heterojunctions. To further analyze photoelectric properties of the as-prepared materials, photoluminescence decays with an excitation wavelength of 450 nm were monitored at 650 nm by time-resolved photoluminescence (TRPL) spectrometer. **Figure 5b** shows PL decay curves modeled by a bi-exponential function comprising a short-lived (τ_1) and a long-lived lifetime (τ_2) component. As listed in **Table S4**, the PL intensity is predominated by the fast decay component with the time constants of τ_1 (3.55 − 14.63 ns), followed by a slower decay (τ_2 = 58.74 − 115.67 ns). The Bi-based hybrid perovskites on glass substrates show the average lifetimes (τ) ranging from 13.91 ns to 37.98 ns. Compared to other samples, the PL lifetime of the heterostructured $MA_3Bi_2I_9/DMA_3BiI_6$ film is significantly enhanced, indicating extended exciton diffusion lifetime due to a reduction of nonradiative recombination in the $MA_3Bi_2I_9/DMA_3BiI_6$ heterojunction,[27] which can have a positive influence on the promotion of H_2 evolution activity arising from efficient charge separation of BBP-5.

To exactly evaluate HI splitting photocatalytic activity, HI was electrochemically reduced for the utilization in the saturated solution in order to remove the originally existing I_3^- in the aqueous system. To determine the origin of the gas component, we used gas chromatography (GC) to measure the H_2 gas at different conditions, i.e., in the absence and presence of Bi-based photocatalysts, as well as the assessment with and without light irradiation. We did not detect any H_2 gas without photocatalysts or under dark condition, verifying that the measured H_2 was

ACCEPTED MANUSCRIPT

completely produced by the photocatalytic reaction under visible light illumination. As shown in **Figure 5c** we clearly confirm that HI can efficiently be split into H_2 and I_3^- by all precipitated Bi-based perovskite photocatalysts under visible-light ($\lambda \geq 420$ nm) illumination, as a result of the suitable band structure (**Figure 4e**). Among them, BBP-5 exhibits the most excellent performance with photocatalytical H_2 production rate of 198.4 μmol per hour per gram, which shows more than 15-fold and 8-fold increases while compared to BBP-0 and BBP-10, respectively. This consequence of visible-light photocatalytic activity is attributed to efficient photogenerated charge carrier separation and transportation induced by the $MA_3Bi_2I_9/DMA_3BiI_6$ heterojunction. In **Figure 3**, the solution color of BBP-5 turns from yellow orange to dark brown after photocatalytic HI splitting reaction, proving the production of I_3^- by BBP-5 photocatalyst without any cocatalyst.

The ultraviolet–visible (UV–Vis) spectra of 1/400 dilution of the solution with deionized water were conducted to quantitatively confirm the production of I_3^- ions under light irradiation (**Figure 5d**). The absorbance peaks at 287 nm and 352 nm increase as the reaction time of photocatalytic processes prolongs, which is corresponding to the absorption spectrum of I_3^-.[28] This reveals that generated I_3^- ions are the product in the oxidation reaction of the photocatalytic HI splitting. Based on the stoichiometry of hydrogen and triiodide productions, we prove that there is no side product in the photocatalytic reaction, as illustrated in **Figure 5e**. Because the photocatalytic HI splitting reaction involves two-electron and two-hole processes to produce one H_2 molecule ($2H^+ + 2e^- \rightarrow H_2$) and one I_3^- ion ($I^- + 2h^+ \rightarrow I_3^-$) respectively,[10] the molar ratio of H_2 to I_3^- theoretically equals to one, resulting in the near-duplicate amount of H_2 and I_3^- during the photocatalytic reaction with BBP-5 photocatalysts (**Figure 5e**). For instance, 41.05 μmol of H_2 and 40.51 μmol of I_3^- were collected under photocatalytic reaction for 120 minutes, and 71.38 μmol of H_2 and 74.64 μmol of I_3^- were detected after photocatalytic reaction for 240 minutes. Because the solution color transformed into dark brown with increasing I_3^- concentration, the light absorption of Bi-based perovskites could be intercepted by evolved I_3^-

ACCEPTED MANUSCRIPT

ions, giving rise to a diminished H_2 evolution rate. A known reducing agent, H_3PO_2, for the reduction reaction from I_3^- back to I^- was added to the saturated HI solution. As confirmed by previous literature,[13] the solution color did not alter and the H_2 evolution rate could persistently be maintained after the addition of H_3PO_2 into the saturated HI solution during photocatalytic reaction. As depicted in **Figure 5f**, the stable solar-driven photocatalytic activity of BBP-5 with the $MA_3Bi_2I_9/DMA_3BiI_6$ heterojunctions can be observed under continuous illumination for 100 hours due to the dynamic equilibrium between the BBP-5 perovskite and the saturated solution.

3. Conclusion

In summary, we have successfully synthesized environmentally friendly Bi-based hybrid perovskites with the $MA_3Bi_2I_9/DMA_3BiI_6$ heterojunction, along with proposed reaction mechanisms by adding different volume percent (vol%) of DMF in IPA solution. The band structures of $MA_3Bi_2I_9$, $MA_3Bi_2I_9/DMA_3BiI_6$ and DMA_3BiI_6 are constructed to explore fundamental properties of heterostructured $MA_3Bi_2I_9/DMA_3BiI_6$ perovskites. The VB and CB positions of $MA_3Bi_2I_9$ and DMA_3BiI_6 show the well-matched type II heterostructure for the formation of an interfacial charge transfer pathway at the interface of $MA_3Bi_2I_9$ and DMA_3BiI_6, giving rise to extended exciton diffusion lifetime with a time constant of ~ 38 ns. It enables more electron transport to reduce H^+ ions, thus promoting photocatalytic hydrogen evolution. The electrochemical reactivity of as-precipitated samples evaluated by an EIS technique reveals that the lowest charge transfer resistances (R_{ct}) of $MA_3Bi_2I_9/DMA_3BiI_6$ is found to be 1.15 kΩ cm^2, which suggests relatively high electrochemical performance, eventually leading to significantly enhanced efficiency and stability of solar-induced hydrogen evolution of $MA_3Bi_2I_9/DMA_3BiI_6$ perovskite heterojunctions without the addition of any noble metal co-catalyst under visible-light irradiation. Consequently, this work presents in-situ formation of hybrid perovskite photocatalysts by heterojunction engineering, which can provide new insights

ACCEPTED MANUSCRIPT

into the development of solar-to-fuel materials for practical applications in the emerging field of hydrogen technology.

4. Experimental Section

Chemicals: All reagents for material synthesis and analysis were purchased and used without further purification. Methylamine iodide (MAI) was obtained from Tokyo Chemical industry (TCI), bismuth nitrate ($Bi(NO_3)_3 \cdot 5H_2O$) was purchased from J&K scientific. Hydroiodic acid (HI) (57 wt% in water; Sigma-Aldrich) was acquired from Energy chemical. Isopropanol (IPA) was received from VWR chemical and N,N-dimethylformamide (DMF) was purchased from ACROS.

Preparation of photocatalysts: The bismuth-based samples were prepared by a simple solvothermal route. 0.2 g of $Bi(NO_3)_3 \cdot 5H_2O$ was dissolved in 30 mL IPA under vigorous stirring, and 0.12 g MAI was then added to the above solution. After the mixture became uniform, 1 mL HI solution as well as a DMF co-solvent at DMF/IPA volume percent of 0%, 1%, 5% and 10% were added for an additional 30 minutes stirring. Thenceforth, the mixture was transferred and sealed into a 50 mL Teflon-lined stainless-steel autoclave. The autoclave reactor was heated at 130oC for 6 hours, and then cooled down to ambient temperature. The resulting precipitates were collected and dried at 60oC for 8 hours. The as-synthesized samples by adding several different amounts of DMF are labeled as bismuth-based perovskite (BBP) – x (x = 0, 1, 5, and 10, where represent the 0, 1, 5, and 10 volume percent (vol%) of DMF in IPA solution respectively).

Characterizations: The X-ray diffraction (XRD) measurements were carried out on powdered materials by using a D8 ADVANCE (Bruker, Fitchburg, WI) instrument equipped with a CuKα radiation source. A Rigaku AFC12 diffractometer with a Mo Kα radiation source was utilized to perform single crystal XRD. UV-visible absorption spectra were recorded on a Shimadzu UV-1800 dual beam absorption spectrophotometer. Photoluminescence (PL)

ACCEPTED MANUSCRIPT

measurements were made on a QuantaMaster 300 fluorimeter (Photon Technology International). Time-resolved PL measurements were made using a time correlated single photon counting setup. A scanning electron microscopy system (SEM, Quanta 650 FEG, FEI Company, Inc., Hillsboro, OR) was used to acquire SEM micrographs. The beam voltage was 2 kV to minimize electron induced damage. X-ray photoelectron spectroscopy (XPS) analysis was studied on a VG ESCALAB MKII with a Mg Kα (1253.6 eV) achromatic X-ray source. Electrochemical impedance spectroscopy (EIS) measurements were carried out using a CH Instruments model 760E electrochemical analyzer as a potentiostat with the AC impedance model. The AC signal had amplitude of 10 mV in the frequency range from 0.1 to 2×106 Hz at zero DC bias. Fourier transform infrared spectroscopy (FT-IR) was recorded on a IRAffinity-1 (Shimadzu) using KBr pellets

Photocatalytic measurements: The photocatalytic hydrogen production experiments in aqueous HI solution were performed in a 50 mL home-made quartz photocatalytic reactor, the openings were sealed with a silicone rubber septum. A 300 W Xenon lamp with a 420 nm cut-off filter was used as a visible light source to trigger the photocatalytic reaction. Hydrogen content was injected and analyzed by gas chromatograph (GC-14C, Shimadzu, Japan, TCD, Ar as a carrier gas and 5 Å molecular sieve column). In the photocatalytic experiment, 100 mg of each photocatalyst was added into 30 mL of saturated HI solution with magnetic stirring. The reaction temperature was maintained at 15°C by a circulating cooling water system. The amounts of evolved H_2 were finally analyzed by the gas chromatograph.

Supporting Information

Supporting Information is available from the Wiley Online Library or from the author.

Acknowledgements

The authors acknowledge financial support from the Research Grants Council of Hong Kong (grant no. 21203518, 8730049 and 9048121), City University of Hong Kong (grant no. 7005289, 9680208, 9667213 and 9052029), Shenzhen Science Technology and Innovation Commission

ACCEPTED MANUSCRIPT

(grant no. R-IND12302), National Natural Science Foundation of China (grant no. 61874165 and 21833009) as well as Major State Basic Research Development Program of China (2019YFB1503401). The authors are grateful to the RGC-PHC France/Hong Kong PROCORE program for the awarding of a bilateral travel grant (project 42544QK)

Received: ((will be filled in by the editorial staff))

Revised: ((will be filled in by the editorial staff))

Published online: ((will be filled in by the editorial staff))

References

[1] a) Y. Bekenstein, B. A. Koscher, S. W. Eaton, P. Yang, A. P. Alivisatos, *Journal of the American Chemical Society* **2015**, 137, 16008; b) A. Swarnkar, R. Chulliyil, V. K. Ravi, M. Irfanullah, A. Chowdhury, A. Nag, *Angewandte Chemie International Edition* **2015**, 54, 15424; c) C. H. Mak, X. Huang, R. Liu, Y. Tang, X. Han, L. Ji, X. Zou, G. Zou, H.-Y. Hsu, *Nano Energy* **2020**, 73, 104752; d) S. Sun, D. Yuan, Y. Xu, A. Wang, Z. Deng, *ACS nano* **2016**, 10, 3648; e) X. Li, F. Cao, D. Yu, J. Chen, Z. Sun, Y. Shen, Y. Zhu, L. Wang, Y. Wei, Y. Wu, *Small* **2017**, 13, 1603996; f) Z. J. Li, E. Hofman, J. Li, A. H. Davis, C. H. Tung, L. Z. Wu, W. Zheng, *Advanced Functional Materials* **2018**, 28, 1704288.

[2] L. Protesescu, S. Yakunin, M. I. Bodnarchuk, F. Krieg, R. Caputo, C. H. Hendon, R. X. Yang, A. Walsh, M. V. Kovalenko, *Nano letters* **2015**, 15, 3692.

[3] B. Saparov, D. B. Mitzi, *Chemical reviews* **2016**, 116, 4558.

[4] a) M. I. Saidaminov, J. Almutlaq, S. Sarmah, I. Dursun, A. A. Zhumekenov, R. Begum, J. Pan, N. Cho, O. F. Mohammed, O. M. Bakr, *ACS Energy Letters* **2016**, 1, 840; b) H.-Y. Hsu, L. Ji, M. Du, J. Zhao, T. Y. Edward, A. J. Bard, *Electrochimica*

ACCEPTED MANUSCRIPT

Acta **2016**, 220, 205; c) S. Seth, A. Samanta, *The journal of physical chemistry letters* **2017**, 8, 4461.

[5] Y. Zhang, M. I. Saidaminov, I. Dursun, H. Yang, B. Murali, E. Alarousu, E. Yengel, B. A. Alshankiti, O. M. Bakr, O. F. Mohammed, *The journal of physical chemistry letters* **2017**, 8, 961.

[6] a) S. González‐Carrero, R. E. Galian, J. Pérez‐Prieto, *Particle & Particle Systems Characterization* **2015**, 32, 709; b) J. Zhao, H. Yin, T. Lim, H. Xie, H.-Y. Hsu, F. Forouzan, A. J. Bard, *Journal of The Electrochemical Society* **2016**, 163, D506; c) E. R. Dohner, A. Jaffe, L. R. Bradshaw, H. I. Karunadasa, *Journal of the American Chemical Society* **2014**, 136, 13154.

[7] J. W. Choi, N. Cho, H. C. Woo, B. M. Oh, J. Almutlaq, O. M. Bakr, S.-H. Kim, C.-L. Lee, J. H. Kim, *Nanoscale* **2019**, 11, 5754.

[8] a) Y. Huang, M. Fang, G. Zou, B. Zhang, H. Wang, *Nanoscale* **2016**, 8, 18734; b) X. Tan, B. Zhang, G. Zou, *Journal of the American Chemical Society* **2017**, 139, 8772.

[9] W. Wang, D. Wang, F. Fang, S. Wang, G. Xu, T. Zhang, *Crystal Growth & Design* **2018**, 18, 6133.

[10] J. Yin, H. Yang, K. Song, A. M. El-Zohry, Y. Han, O. M. Bakr, J.-L. Brédas, O. F. Mohammed, *The journal of physical chemistry letters* **2018**, 9, 5490.

[11] a) Z. Chen, H.-Y. Hsu, M. Arca, K. S. Schanze, *The Journal of Physical Chemistry B* **2014**, 119, 7198; b) T.-H. Lai, I. Constantinou, C. M. Grand, E. D. Klump, S. Baek, H.-Y. Hsu, S.-W. Tsang, K. S. Schanze, J. R. Reynolds, F. So, *Chemistry of Materials* **2016**, 28, 2433; c) I. Constantinou, T. H. Lai, H. Y. Hsu, S. H. Cheung, E. D. Klump, K. S. Schanze, S. K. So, F. So, *Advanced Electronic Materials* **2015**, 1, 1500167.

[12] R. A. Marcus, *Reviews of Modern Physics* **1993**, 65, 599.

[13] a) L. S. Devi, M. K. Al-Suti, C. Dosche, M. S. Khan, R. H. Friend, A. Köhler, *Physical Review B* **2008**, 78, 045210; b) X. Zou, L. Ji, H.-Y. Hsu, K. Zheng, Z. Pang,

ACCEPTED MANUSCRIPT

X. Lu, *Journal of Materials Chemistry A* **2018**, 6, 12724; c) J.-L. Brédas, D. Beljonne, V. Coropceanu, J. Cornil, *Chemical Reviews* **2004**, 104, 4971.

[14] R. A. Marcus, *The Journal of chemical physics* **1956**, 24, 966.

[15] a) S. J. Su, E. Gonmori, H. Sasabe, J. Kido, *Advanced Materials* **2008**, 20, 4189; b) W. Li, Y. Pan, L. Yao, H. Liu, S. Zhang, C. Wang, F. Shen, P. Lu, B. Yang, Y. Ma, *Advanced Optical Materials* **2014**, 2, 892; c) X. de Vries, R. Coehoorn, P. A. Bobbert, *Nature communications* **2020**, 11, 1.

[16] A. J. Bard, L. R. Faulkner, J. Leddy, C. G. Zoski, *Electrochemical methods: fundamentals and applications*, wiley New York, **1980**.

[17] D. D. Perrin, W. Armarego, D. R. Perrin, *Purification of Laboratory Chemicals, by DD Perrin. WLF Armarego and Dawn R. Perrin*, Pergamon Press, **1966**.

[18] D. Diamond, *Trends in Analytical Chemistry* **1996**, 1, X.

[19] J. Wang, *Inc., New York* **2000**, 81.

[20] N. K. Bhatti, M. S. Subhani, A. Y. Khan, R. Qureshi, A. Rahman, *Turkish Journal of Chemistry* **2006**, 29, 659.

[21] N. K. Bhatti, M. S. Subhani, A. Y. Khan, R. Qureshi, A. Rahman, *Turkish Journal of Chemistry* **2006**, 30, 165.

[22] H. Qi, Y.-H. Chen, C.-H. Cheng, A. J. Bard, *Journal of the American Chemical Society* **2013**, 135, 9041.

[23] M. Shen, J. n. Rodríguez-López, J. Huang, Q. Liu, X.-H. Zhu, A. J. Bard, *Journal of the American Chemical Society* **2010**, 132, 13453.

[24] T.-I. Ho, A. Elangovan, H.-Y. Hsu, S.-W. Yang, *The Journal of Physical Chemistry B* **2005**, 109, 8626.

[25] P. J. Smith, C. K. Mann, *The Journal of Organic Chemistry* **1969**, 34, 1821.

[26] M. Shen, J. n. Rodríguez-López, Y.-T. Lee, C.-T. Chen, F.-R. F. Fan, A. J. Bard, *The Journal of Physical Chemistry C* **2010**, 114, 9772.

ACCEPTED MANUSCRIPT

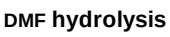
The heterojunctions of $MA_3Bi_2I_9$ and DMA_3BiI_6 hybrid perovskites are constructed using a dimethylformamide (DMF)-assisted solvent-engineering technique, resulting in enhanced solar HI splitting efficiency without any metal co-catalyst. An in-situ formation of perovskite photocatalysts by heterojunction engineering opens a new avenue in the field of solar energy conversion technologies.

.

Keyword: in-situ formation, perovskite heterojunction, co-catalyst-free, photocatalytic hydrogen evolution

Yunqi Tang, Chun Hong Mak, Rugeng Liu, Xu Han, Zuankai Wang, Haisheng Song, Chunyan Tang, Frédéric Barrière and Hsien-Yi Hsu*

In-situ formation of bismuth-based perovskite heterostructures for high-performance co-catalyst-free photocatalytic hydrogen evolution



ACCEPTED MANUSCRIPT

Copyright WILEY-VCH Verlag GmbH & Co. KGaA, 69469 Weinheim, Germany, 2016.

Supporting Information

In-situ formation of bismuth-based perovskite heterostructures for high-performance co-catalyst-free photocatalytic hydrogen evolution

Yunqi Tang, Chun Hong Mak, Rugeng Liu, Xu Han, Zuankai Wang, Haisheng Song, Chunyan Tang, Frédéric Barrière and Hsien-Yi Hsu*

Table S1. Crystal data and structure refinement for $MA_3Bi_2I_9$ (BBP-0).

Crystal data	Details
Empirical Formula	$C_3H_{18}Bi_2I_9N_3$
Formula Weight	1413.42
Temperature (K)	233
Crystal system	Hexagonal
Space group	P63/mmc
Unit cell dimensions	a=8.58Å
	b=8.58Å
	c=21.69Å
Volume (Å)	1382.8
Z	2
Density (g/cm^3)	3.974

Table S2. Crystal data and structure refinement for DMA_3BiI_6 (BBP-10).

Crystal data	Details
Empirical Formula	$C_6H_{24}BiI_6N_3$
Formula Weight	1108.66
Temperature (K)	233
Wavelength	1.54178
Crystal system	Rhomboedric
Space group	$R\bar{3}$
Unit cell dimensions	a=30.75 (Å)
	b=30.75(Å)
	c=8.79(Å)
Volume (Å)	7203.7
Z	12
Density (g/cm^3)	3.067

ACCEPTED MANUSCRIPT

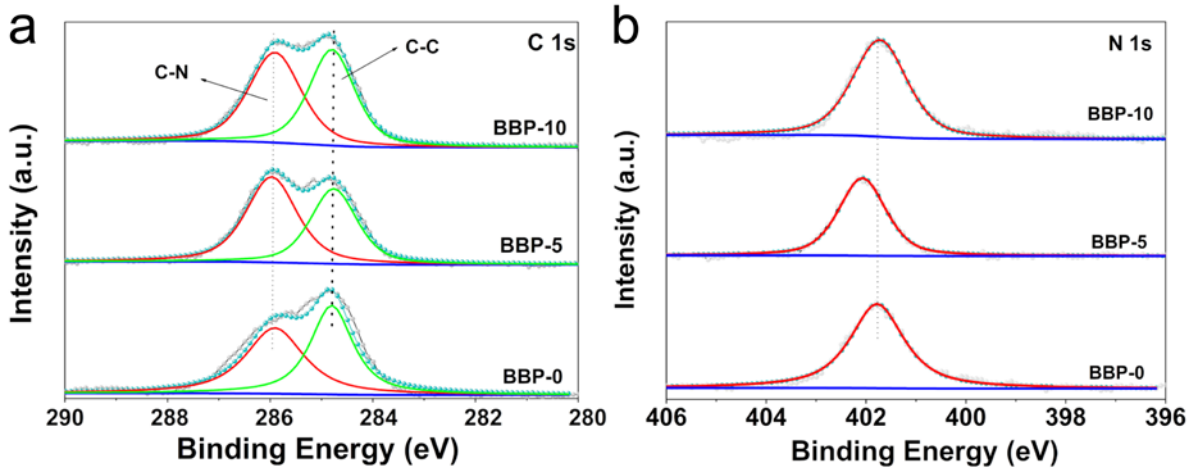


Figure S1. High resolution X-ray photoelectron spectroscopy (XPS) spectra of (a) C 1s and (b) N 1s regions for BBP-0, BBP-5 and BBP-10.

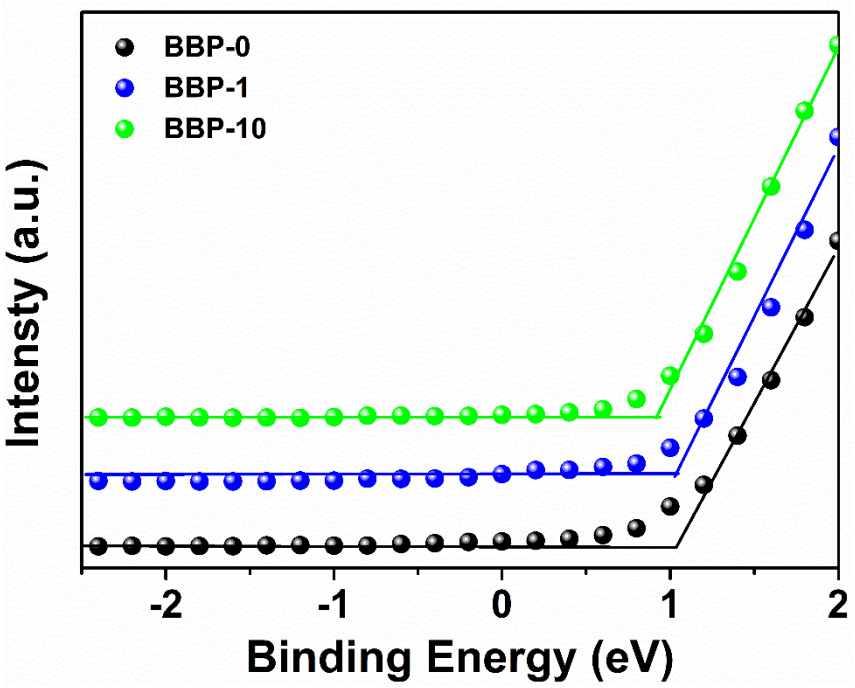


Figure S2. Linear analysis applied to the XPS valence band of the BBP-0, BBP-1 and BBP-10 powders.

ACCEPTED MANUSCRIPT

Table S3. Fitted parameters extracted from the Nyquist plots of all prepared sample electrodes.

Sample	Rs (Ω cm^2)	Rct (Ω cm^2)	CPE$*10^8$ (F cm^{-2})
BBP-0	191.3	1324	1.79
BBP-1	185.1	1279	0.72
BBP-5	147.8	1151	0.82
BBP-10	172.2	1280	0.89

Table S4. PL decay kinetics of all as-prepared samples.

Sample	$\tau1$/ns(α_1)	$\tau2$/ns(α_2)	$<\tau>^a$/ns	χ^2
BBP-0	58.74 (18.74%)	3.55 (81.26%)	13.91	0.74
BBP-1	83.44 (21.68%)	8.65 (78.32%)	24.87	0.94
BBP-5	115.67 (23.11%)	14.63 (76.89%)	37.98	0.9
BBP-10	65.94 (22.77%)	5.98 (77.23%)	19.63	0.95

[a] $\langle\tau\rangle = \sum_i \alpha_i \tau_i$



Figure S3. Optical photograph of the reaction solution of BBP-5 without any cocatalysts before (left) and after (right) photocatalytic HI splitting reaction.

ACCEPTED MANUSCRIPT

Table S5. Photocatalytic performance and cycle stability of various photocatalysts under different experimental conditions

Material	Co-catalyst	Stability (h)	Performance ($\mu mol \cdot g^{-1} h^{-1}$)	Ref.
$MA_3Bi_2I_9/DMA_3BiI_6$	−	100	198.4	This work
$MA_3Bi_2I_9$	−	−	12.3	This work
DMA_3BiI_6	−	−	24.5	This work
$MA_3Bi_2I_9$	$H_2PtCl_6 \cdot 6H_2O$	70	169.21	[1]
$MA_3Bi_2I_9$	−	−	12.19	[1]
$MAPbI_3$	$H_2PtCl_6 \cdot 6H_2O$	160	57	[2]
$MAPbI_3$/rGO	$H_2PtCl_6 \cdot 6H_2O$	400	93.9	[3]
PtI_x/DMA_3BiI_6	$H_2PtCl_6 \cdot 6H_2O$	100	142	[4]
DMA_3BiI_6	−	−	15.16	[4]
$MAPbI_3/Pt/TiO_2$	Pt	12	29.8	[5]

References

1. Guo, Y., et al., *Stable Lead-Free (CH3NH3) 3Bi2I9 Perovskite for Photocatalytic Hydrogen Generation.* ACS Sustainable Chemistry & Engineering, 2019. **7**(17): p. 15080-15085.
2. Park, S., et al., *Photocatalytic hydrogen generation from hydriodic acid using methylammonium lead iodide in dynamic equilibrium with aqueous solution.* Nature Energy, 2017. **2**(1): p. 16185.
3. Wu, Y., et al., *Composite of CH3NH3PbI3 with reduced graphene oxide as a highly efficient and stable visible-light photocatalyst for hydrogen evolution in aqueous HI solution.* Advanced Materials, 2018. **30**(7): p. 1704342.
4. Zhao, H., et al., *PtIx/[(CH3) 2NH2] 3 [BiI6] as a well-dispersed photocatalyst for hydrogen production in hydroiodic acid.* Nano energy, 2018. **50**: p. 665-674.
5. Wang, X., et al., *Dynamic interaction between methylammonium lead iodide and TiO2 nanocrystals leads to enhanced photocatalytic H2 evolution from HI splitting.* ACS Energy Letters, 2018. **3**(5): p. 1159-1164.

ACCEPTED MANUSCRIPT